

PAPER • OPEN ACCESS

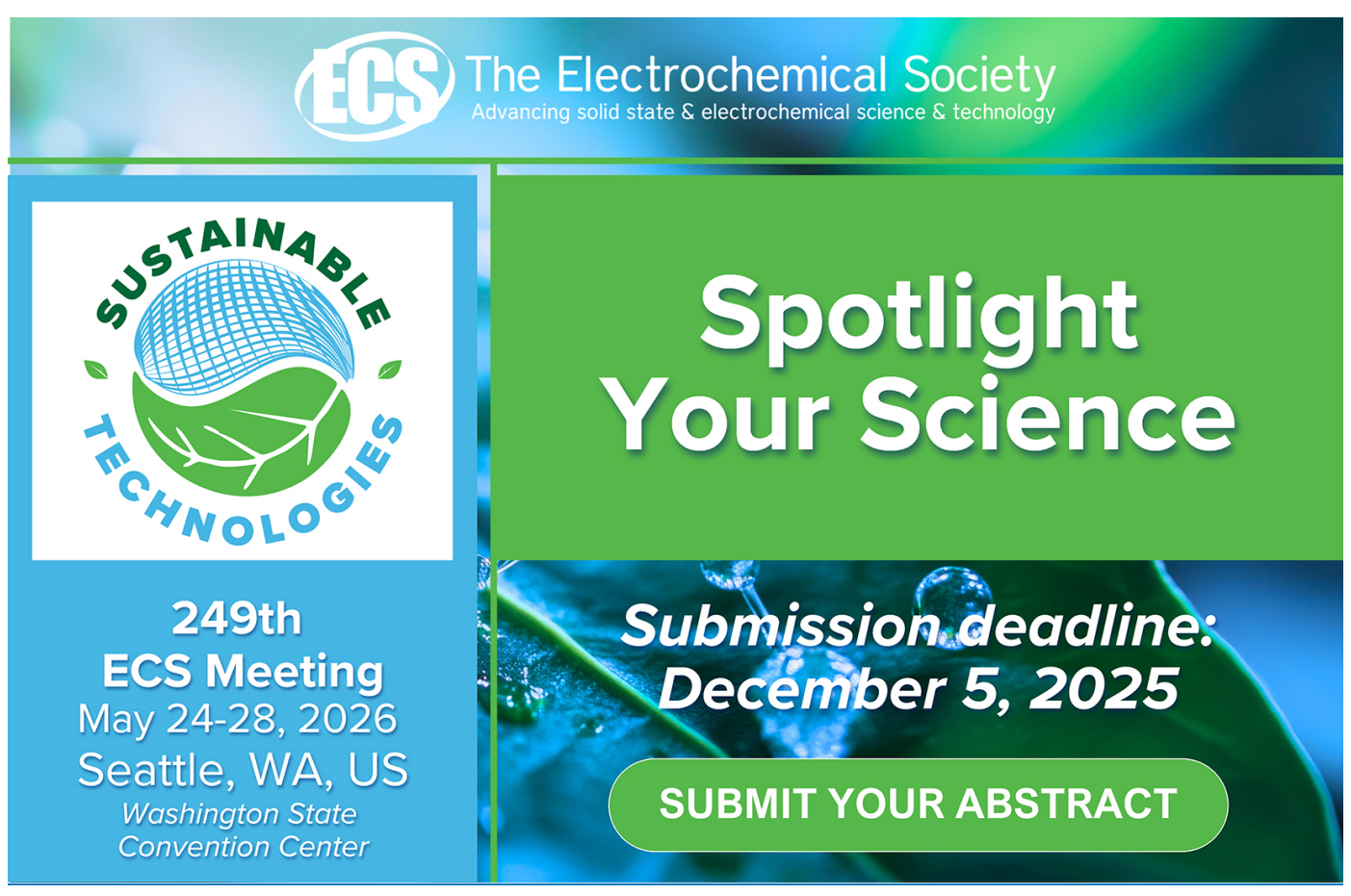
Platanus occidentalis L. fruit-derived carbon materials for electrochemical potassium storage

To cite this article: Jiaxing Hao et al 2025 Nanotechnology 36 125701

View the <u>article online</u> for updates and enhancements.

You may also like

- High performance Mg–Li dual metal-ion batteries based on highly pseudocapacitive hierarchical TiO₂-B nanosheet assembled spheres cathodes Mewin Vincent, Venkata Sai Avvaru, Maciej Haranczyk et al.
- Electroisomerization blinking of an azobenzene derivative molecule Sylvie Godey, Hugo Therssen, David Guérin et al.
- Surface receptor-targeted protein-based nanocarriers for drug delivery: advances in cancer therapy
 Panneerselvam Theivendren,
 Parasuraman Pavadai, Suganthan
 Veerachamy et al.



Nanotechnology 36 (2025) 125701 (9pp)

Platanus occidentalis L. fruit-derived carbon materials for electrochemical potassium storage

Jiaxing Hao^{1,6}, Mingyuan Ye^{2,6}, Ajay Piriya Vijaya Kumar Saroja³, Liying Liu¹, Yuhan Wu^{2,4,*}, Xiaorui Hao⁵, Feng Liu¹, Yingjiao Fang¹, Xuejun Dong⁴, Laishi Li¹, Yusheng Wu^{1,*} and Yang Xu^{3,*}

E-mail: yuhanwu@sut.edu.cn, wuyus@sut.edu.cn and y.xu.1@ucl.ac.uk

Received 1 September 2024, revised 16 December 2024 Accepted for publication 10 January 2025 Published 23 January 2025



Abstract

In the post-lithium-ion battery era, potassium-ion batteries (PIBs) have been considered as a promising candidate because of their electrochemical and economic characteristics. However, as an emerging electrochemical storage technology, it is urgent to develop capable anode materials that can be produced at low cost and on a large scale to promote its practical application. Biomass-derived carbon materials as anodes of PIBs exhibit strong competitiveness by their merits of low weight, high stability, non-toxicity, and wide availability. In this work, we employed Platanus occidentalis L. fruits as a precursor to prepare a series of biomass-derived carbon materials by simply adjusting carbonization temperature, and we explored their electrochemical potassium storage capability as anode materials. The optimized sample (annealed at 800 °C) delivered good potassium storage capability (193.3 mAh g⁻¹ at 100 mA g⁻¹ after 100 cycles), cycling stability (80.4 mAh g⁻¹ after 300 cycles at 300 mA g⁻¹), and rate performance (51.2 mAh g⁻¹ at 1000 mA g⁻¹). This work demonstrates a feasible way to utilize biomass waste disposal for emerging sustainable energy storage technologies.

Supplementary material for this article is available online

Keywords: sustainable, cost-effective, biomass, potassium-ion batteries, carbon, defect

^{*} Authors to whom any correspondence should be addressed.



Original content from this work may be used under the terms of the Creative Commons Attribution 4.0 licence. Any fur-

¹ School of Materials Science and Engineering, Shenyang University of Technology, Shenyang 110870, People's Republic of China

² School of Environmental and Chemical Engineering, Shenyang University of Technology, Shenyang 110870, People's Republic of China

³ Department of Chemistry, University College London, London WC1H 0AJ, United Kingdom

⁴ School of Chemistry and Chemical Engineering/State Key Laboratory Incubation Base for Green Processing of Chemical Engineering, Shihezi 832003, People's Republic of China

School of System Design and Intelligent Manufacturing, Southern University of Science and Technology, Shenzhen 518055, People's Republic of China

⁶ These authors are contributed equally to this work.

1. Introduction

The energy and environmental problems caused by the high consumption of conventional fossil fuels drive the rapid development of the electrochemical energy storage market represented by lithium-ion batteries (LIBs) with high energy densities, long cycle life, and environmental friendliness [1–9]. However, the scarcity (~20 ppm) and uneven distribution (~70% in South America) of lithium sources on the earth's crust limit their large-scale production and stable supply [10– 13]. It is estimated that LIBs will consume 65% of total lithium consumption by 2025. Besides, based on lithium consumption rates projected for 2050, the remaining lithium reserves on land will only last until 2080 [14]. In this case, many new types of metal ion battery technologies (e.g. sodium-, potassium-, zinc-, magnesium-, and calcium-ion batteries) have been launched successively as supplements or alternatives to LIBs [15]. Recently, potassium-ion batteries (PIBs) as a member of alkali metal-ion batteries have captured increasing attention. They possess many electrochemical properties similar to LIBs. Meanwhile, their cost-effectiveness and abundant K resources endow them with strong competitiveness [16].

In a metal ion battery, the anode plays a crucial role in the safety and lifespan of the battery [17]. Currently, a variety of materials have been investigated as PIB anodes, including carbon materials, metal oxides/chalcogenides/phosphides, alloying-based materials, and organic materials [18-20]. Among them, carbon materials are considered to be promising candidates because of their superior material and electrochemical properties, low weight, and environmental friendliness [17]. Biochar is a kind of carbon material obtained by the thermal decomposition of biomasses (e.g. plants, animal wastes, and microorganisms) under anoxic or limited oxygen conditions [21, 22]. Biochar has been widely used as an electrochemical energy storage material, benefiting from the renewability and environmental friendliness of biomass resources. To achieve practical applications and large-scale production, it is of great significance to explore low-cost and high-yield biomass precursors to produce biochar as PIB

Platanus occidentalis L. is native to North America and is widely planted in the United States, China, Argentina, Australia, and other places [23]. However, Platanus occidentalis L. bears a lot of fruit (named POF) every year, which forms a large amount of pollen in spring and summer. In the meantime, the dehiscence of the fruit produces a large amount of POF lint, which may cause fire risks and can easily enter the respiratory tract of human beings, leading to allergic reactions and various other diseases in some people. Therefore, how to deal with POF in a green and valuable manner has received special attention. Herein, we prepared carbon materials using POF as the precursor by a two-step pyrolysis process and investigated the electrochemical performance of the carbons as PIB anodes. The results showed that the specific capacities of the optimized sample were 194 mAh g⁻¹ after 100 cycles at 0.1 A g⁻¹ and 80.4 mAh g⁻¹ after 300 cycles at $0.3~A~g^{-1}$. Our work provides a feasible way to efficiently utilize POF waste in line with the concept of sustainable development and prepares a promising PIB anode material for large-scale production.

2. Experimental section

2.1. Materials preparation

The POF precursor exhibits a tubular shape (**figure** (**S1**)). It was firstly pulverized into powers, and then, the powders were washed with deionized water for several times, followed by drying in a vacuum oven at 80 °C. Subsequently, the dried powders were annealed at 400 °C with a heating rate of 5 °C min⁻¹ for 2 h under an Ar atmosphere. The pre-treated material was then annealed at different temperatures (600, 800, and 1000 °C) with a heating rate of 5 °C min⁻¹ for 2 h under an Ar atmosphere. The carbonized powders were washed with deionized water and hydrochloric acid for several times. The final products were obtained after drying and denoted as WT-600, WT-800, and WT-1000, respectively. The preparation method is schematically shown in figure 1(a).

2.2. Materials characterizations

Morphology and microstructure of the products were observed by scanning electron microscopy (SEM, Carl Zeiss Jena GeminiSEM300), transmission electron microscope (TEM, JEM-2100), and selected area electron diffraction (SAED, FEI Tecnai F20). Phase was analyzed by x-ray diffractometer (XRD, Shimadzu x-ray 7000 with Cu K α radiation, $\lambda = 1.54056$ Å). Surface chemical information was investigated by x-ray photoelectron spectroscopy (XPS, Thermo Scientific K-Alpha). Chemical bonding information was recorded by Raman spectroscopy (HORIBA Horiba LabRAM HR Evolution).

2.3. Electrochemical measurements

Working electrodes were prepared by mixing the WT sample, acetylene black, and carboxymethyl cellulose sodium (CMC) with a weight ratio of 8:1:1. The mass loading was 1-2 mg cm⁻². Then, the electrode was dried at 105 °C under vacuum overnight. Electrochemical property evaluation was carried out using CR2032-type coin cells assembled in an Ar-filled glovebox with oxygen and moisture concentrations below 0.1 ppm. K foil was used as a counter electrode and separated from the working electrode by a glass fiber membrane (Whatman, Grade GF/B). The electrolyte was 0.8 M KPF₆ in ethylene carbonate/diethyl carbonate (EC/DEC 1:1 Vol%). Galvanostatic discharge/charge (GDC) measurements were performed on a battery testing system (LANHE CT2001A) in a voltage range of 0.01 - 3.0 V at room temperature. Cyclic voltammetry (CV), electrochemical impedance spectroscopy (EIS), and electrochemical galvanostatic intermittent titration

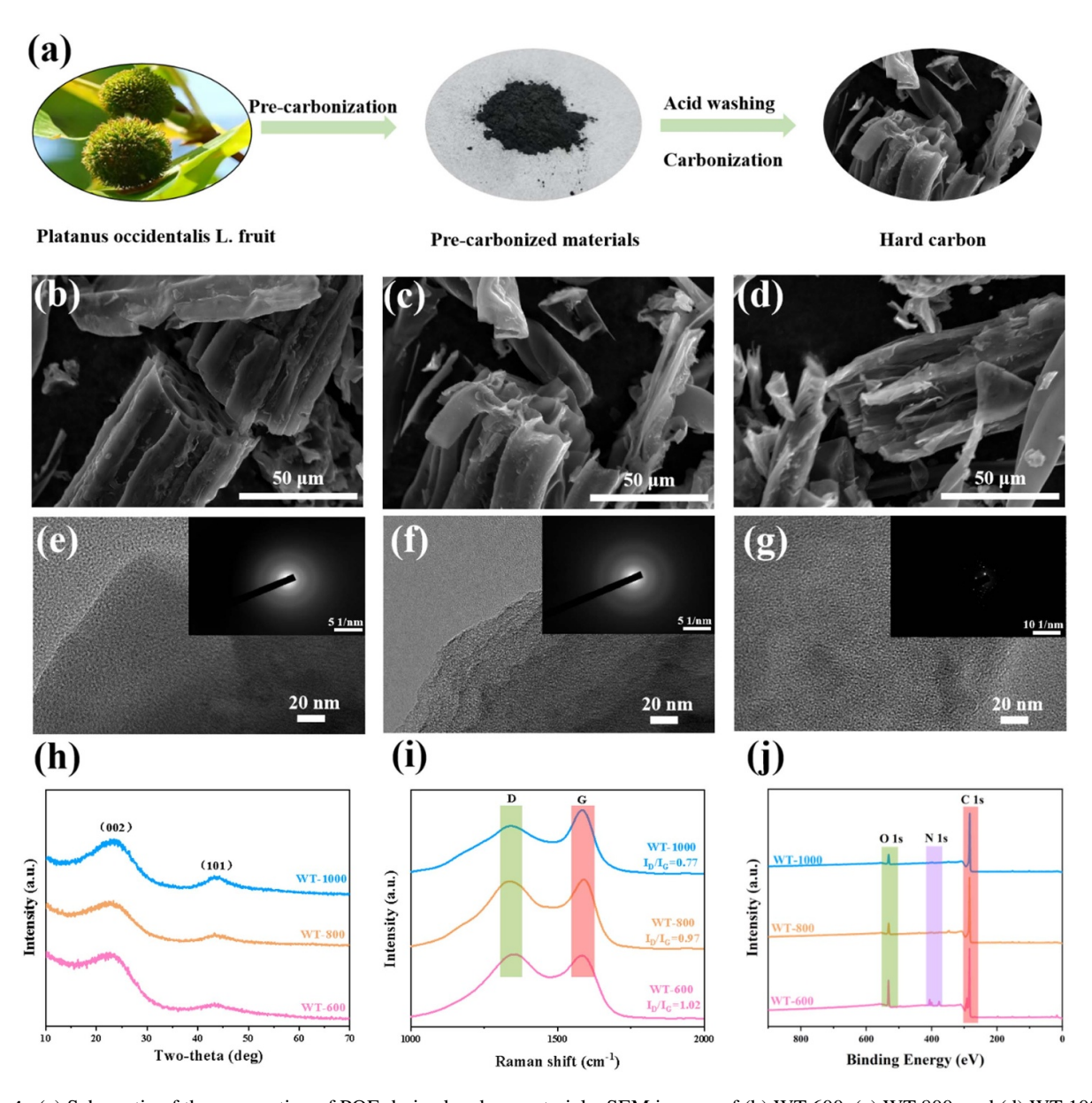


Figure 1. (a) Schematic of the preparation of POF-derived carbon materials; SEM images of (b) WT-600, (c) WT-800, and (d) WT-1000; TEM and SAED images of (e) WT-600, (f) WT-800, and (g) WT-1000; (h) XRD patterns, (i) Raman spectrum, and (j) XPS survey spectra of the carbon materials.

(GITT) measurements were carried out on an electrochemical workstation (DH7002A). As for full cells assembled by employing WT-800 as the anode and commercial perylene-3,4,9,10-tetracarboxylic dianhydride (PTCDA), the voltage range is 0.8–3.2 V. The mass loading of PTCDA was 2–3 mg cm⁻². The mass ratio of PTCDA:WT-800 was 2.5:1.

3. Results and discussion

3.1. Material characterizations

To determine the morphological features of POF-derived carbon materials, the obtained WT-600, WT-800, and WT-1000 were characterized by SEM, as displayed in figures 1(b)–(d)

and (S2). POF-derived carbon materials exhibit a porous tubular structure with nano-sized walls [24], which is conducive to infiltrating the electrolytes, buffering the volume expansion, and shortening the diffusion distance of K^+ [25]. Figure (S2) is a SEM image of WT-800, showing that the hole wall thickness is about 1.5 μ m and the inner diameter is 20–30 μ m. There is no significant change as the annealing temperature increases. TEM and SAED were utilized to reveal the effect of carbonation temperature on the structural properties of the WT samples (figures 1(e)–(g)). As the annealing temperature increases, the graphitization degree of the carbon material gradually increases [26]. Also, the ring diffraction patterns (in the inserts of figures 1(e)–(g)) become less diffusive as the temperature increases, and a large number of continuous pseudo-graphite domains are formed in WT-1000 (figure

(S3)), which show crystalline properties and can be observed in a clear diffraction pattern when the temperature reaches $1000\,^{\circ}\text{C}$.

The structural properties of the POF-derived carbon materials were further investigated using XRD and Raman measurements. In the XRD patterns shown in figure 1(h), two broad diffraction peaks are located near 23 and 43° in the three samples, corresponding to the (002) and (101) planes of amorphous carbon, respectively [27, 28]. The (002) peak gradually moves to the larger 2θ angle as the carbonization temperature increases, signifying a progressive reduction in the layer spacing. Based on the Bragg Law, the layer spacings of WT-600, WT-800, and WT-1000 were calculated to be 0.39, 0.38, and 0.37 nm, respectively. They are all higher than that of graphite (0.335 nm), a commercial anode material of PIBs, which is in favor of promoting the intercalation of K⁺ in the graphite crystallite structure [29]. The graphitization degree of WTs is revealed by Raman spectroscopy, as presented in figure 1(i). Two obvious peaks appear at 1333 and 1588 cm⁻¹, corresponding to the disorder-induced Dband and in-plane vibrational G-band, respectively. The disorder degree of WTs is represented by the intensity ratio (I_D/I_G) of the D-band to the G-band [30]. The I_D/I_G values of WT-600, WT-800, and WT-1000 are 1.02, 0.97, and 0.77, respectively, showing a gradually decreasing trend [31]. This demonstrates that increasing the carbonization temperature can improve the graphitization degree of POF-derived carbon materials [32]. In addition, the I_D/I_G values of WT-600 and WT-800 are close to 1.0, indicating a high disorder degree and high defect concentration; therefore, there are abundant active sites for the K⁺ storage, resulting in an enhanced capacity. The N₂ adsorption-desorption isotherms shown in **figure** (S4) indicate that BET specific surface areas of POF-derived carbon materials are 315.878, 290.334, and 1.301 $\text{m}^2\text{ g}^{-1}$ at calcination temperatures of 600, 800, and 1000 °C, respectively. The decreased specific surface with increasing carbonization temperature is mainly due to pore shrinkage induced by high carbonization temperature. XPS was performed to analyze the surface chemical composition of WTs. The survey spectra (figure 1(j)) reveal that WTs mainly consist of C and O, with a small amount of N. As the calcination temperature increases, the contents of O and N gradually decrease and tend to be stable, as shown in table (S1). The oxygen reduction can be attributed to dehydration (the reaction between C-H and C-OH), decarboxylation (the decomposition of -COOH), and decarbonylation (the decomposition of C=O) (figure (S5)) [33]. As for nitrogen reduction, it is mainly caused by the pyrolysis or decomposition of nitrogen-rich compounds, releasing N-containing gases such as NH3 and N₂ [34]. The increased C content can increase the active proportion of electrode materials, the decreased O content can reduce the less reversible storage of K⁺ by oxygen-containing functional groups [35, 36], and the presence of N can produce abundant defects on the surface of the material, providing storage sites and diffusion channels for K⁺ and enhancing the conductivity.

3.2. Electrochemical investigation

The potassium storage performance of WTs as anodes was investigated by CV tests in half cells with a potential window of 0.01–3.0 V. Figures 2(a) and (S6) depict the CV curves of the initial three cycles at a scan of 0.1 mV s⁻¹. A reduction peak can be observed at about 0.75 V in the first cycle and disappears in subsequent cycles. The cause of this irreversible occurrence is the electrolyte consumption during the formation of solid-electrolyte interface (SEI) [18, 37, 38]. The peak at \sim 0.01 V in the first cycle corresponds to the K⁺ insertion into the graphitic layers, while the peak at about 0.5 V corresponds to the K⁺ detachment from the graphitic layers. The nearly overlapping second and third CV curves indicate that WTs have good reversibility. This can also be verified by the well-overlapped GCD profiles at a current density of 0.1 A g^{-1} (figures 2(b) and (S7)). The WT-800 electrode delivers initial discharge and charge capacities of 367.4 and 234.2 mAh g⁻¹, respectively, corresponding to an initial Coulombic Efficiency (ICE) of 63.7%, which is higher than that of WT-600 (59.0%) and WT-1000 (60.3%). The relatively low ICEs are attributed to the formation of SEI layers, but fortunately, CEs increase to \sim 95% in the second cycle. Although the specific surface areas of WT-600 and WT-800 are similar, the abundance of defects and oxygen-containing functional groups in the WT-600 can cause side reactions with K⁺ and lead to irreversible potassium loss, resulting in a more significant loss of initial capacity during cycling. As for WT-1000, it has a higher graphitization degree, which increases the contribution of insertion capacity in the graphite layer, leading to irreversible insertion of K⁺, thus affecting ICE. The synergistic effect originated from the structural properties may result in the higher ICE of WT-800, such as appropriate specific surface area, defect concentration, graphitization degree and heteroatom contents [39].

The cycling performance of the WT electrodes was evaluated to determine the effect of carbonization temperature on the potassium storage performance of the POF-derived carbon materials. As shown in figure 2(c), the WT-800 electrode delivers the highest discharge capacity and retains 220.7, 197.6, and 193.3 mAh g⁻¹ after 10, 50, and 100 cycles at 0.1 A g⁻¹, respectively. The WT-600 and WT-1000 electrodes only maintain 128.7 mAh g⁻¹ and 128.4 mAh g⁻¹ after 100 cycles at 0.1 A g⁻¹, respectively. The similar cycling tendencies of WT-600 and WT-1000 are due to the excessive number of defects or graphite units that make it difficult to achieve rapid electron/ion migration simultaneously. WT-600 consists mainly of many disordered structures, which, even though this structure is favorable for the storage of K⁺, lacks electron transfer pathways and is poorly conductive, and WT-1000 contains a large number of contiguous pseudo-graphite domains, which indicate an increase in conductivity, but restricted ion diffusion. WT-800 has an appropriate graphitization/defect ratio, which leads to good cycling performance. The fast charge/discharge capability of the WT electrodes was evaluated using a rate performance test (figure 2(e)). WT-800 exhibits higher discharge

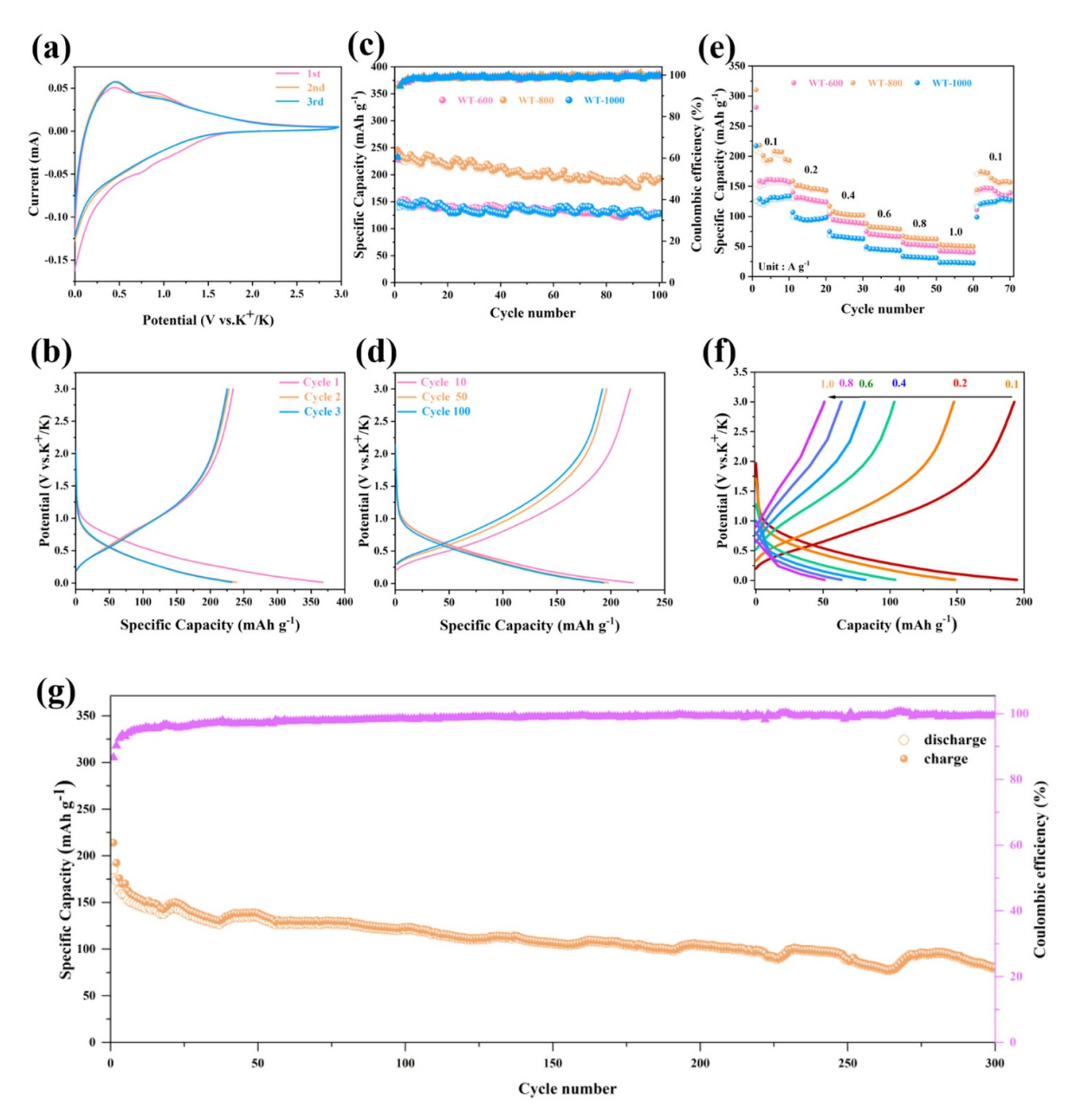


Figure 2. Electrochemical performance of the prepared WT samples. (a) CV curves of the initial three cycles of WT-800; (b) GCD profiles of the initial three cycles of WT-800 at a current density of 0.1 A g^{-1} ; (c) cycling performance of WTs at 0.1 A g^{-1} ; (d) GCD profiles of WT-800 at 0.1 A g^{-1} ; (e) rate performance of WTs; (f) GCD profiles of WT-800 at various current densities; (g) cycling performance of WT-800 at 0.3 A g^{-1} .

capacities at each current density. The average discharge capacities of WT-800 are 212.8, 148.6, 105.1, 81.7, 63.9, and 51.2 mAh g⁻¹ at 0.1, 0.2, 0.4, 0.6, 0.8, and 1.0 A g⁻¹. As for WT-600 and WT-1000, their discharge capacities are only 41.5 and 23.2 mAh g⁻¹ at 1.0 A g⁻¹, respectively. The appropriate graphitization/defect ratio enables fast electron and ion transport. The GCD profiles of WT-800 at various current densities preserve similar shapes, further confirming its good rate capability (figure 2(f)). Cycling performance of WT-800 at a high current density is presented in figure 2(g). It maintains a discharge capacity of 80.4 mAh g⁻¹ after 300 cycles at 0.3 A g⁻¹.

To investigate the potassium storage kinetics and mechanisms of WT-800, CV measurements were carried out at various scan rates from 0.1 to 1.0 mV s⁻¹. The CV curves present similar outlines. The redox peak current increases and the peak region occupies higher voltage areas with the growth of scan rates, indicating the existence of surface-controlled behavior (figure 3(a)) [40, 41]. Generally, the current (i) and scan rate (v) follow a power law relationship (equation (1)).

$$i = av^b \tag{1}$$

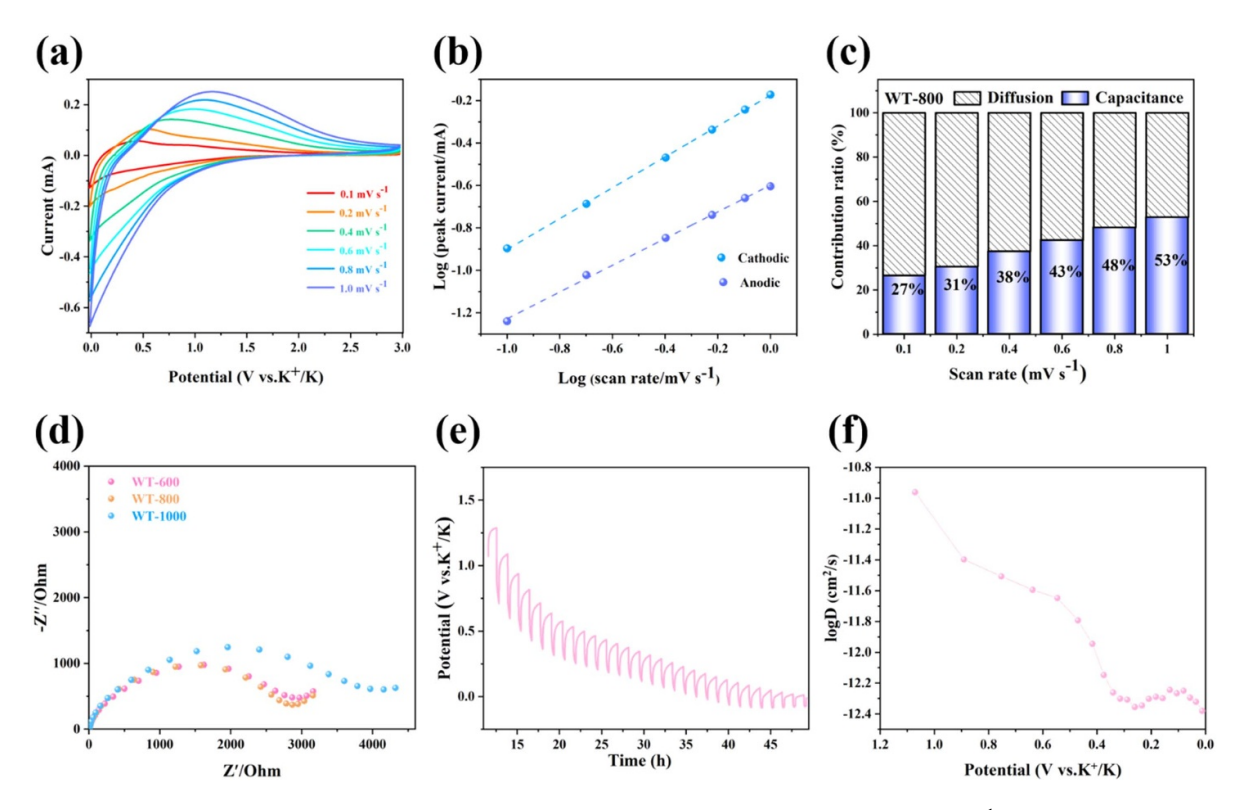


Figure 3. Reaction kinetic investigation. (a) CV curves at various scan rates ranging from 0.1 to 1.0 mV s⁻¹; (b) a functional relationship between the peak current (i) and scan rate (v); (c) capacitive contribution ratios (blue/white) at different scan rates; (d) EIS spectra of the WT electrodes after the initial cycle; (e) GITT profile and (f) D_k of WT-800 as a function of discharge processes.

where a and b are variable constants. Furthermore, b can be determined by plotting $\log(i)$ against $\log(\nu)$ (equation (2)).

$$\log(i) = b\log(v) + \log(a). \tag{2}$$

Different *b*-value ranges in electrochemical reactions correspond to different kinetic control processes [42, 43]. The electrochemical reaction is governed by ion diffusion when the *b*-value is around 0.5, while capacitive behaviors dominate when the *b*-value approaches 1.0 [44, 45]. The electrochemical process appears to be mainly dependent on ion diffusion because the calculated *b*-values are 0.63 and 0.73 at the anodic and the cathodic peaks of WT-800, respectively (figure 3(b)). To further quantify the contribution of different behaviors, the current response (*i*) at a fixed potential (*V*) is split into capacitive effect (k_1v) and ion diffusion process ($k_2v^{1/2}$) (equations (3) and (4)).

$$i(V) = k_1 v + k_2 v^{1/2} (3)$$

$$i/v^{1/2} = k_1 v^{1/2} + k_2 (4)$$

where k_1 and k_2 are constants. The calculated capacitive contribution of WT-800 is 43% at 0.6 mV s⁻¹ (**figure (S8)**) and increases to 48% at 1.0 mV s⁻¹ (figure 3(c)) [46]. Fast electrochemical reaction kinetics is achieved by clear diffusion-controlled features of WT-800, which could be strongly correlated with its amorphous structure, good pore structure, and appropriate graphitization/defect ratio.

The charge transfer kinetics of WTs was explored using EIS measurements. Figure 3(d) depicts the Nyquist plots of the WT electrodes after one cycle. The plots consist of a semicircle in the mid- and high-frequency regions (charge transfer resistance, R_{ct}) and a straight line in the low-frequency region (Warburg resistance, W_0) [47]. The equivalent circuit for EIS data fitting is shown in **figure** (S9), and the fitting results are given in **table (S2)**. WT-800 has the lowest R_{ct} (2506 Ω), indicating better charge transfer kinetics during discharge processes. K^+ diffusion coefficient (D_k) was evaluated during the discharge process using the GITT technique to further elucidate the kinetics of WT-800 (the detailed calculation method of D_k is shown in **figure** (S10). A potentiation settling process with a pulse of 15 min and a relaxation of 1 h at 0.05 A g^{-1} is depicted in figure 3(e). The calculated D_k values are presented in figure 3(f). As a consequence of the surface capacitive behavior in the high voltage region (>0.4 V) and the diffusion process in the low voltage region (<0.4 V), the D_k of the WT-800 electrode decays rapidly in the former and slowly in the latter.

Ex situ Raman results of the WT-800 electrode during the first cycles are displayed in figures 4(a) and (b). The I_D/I_G value increases gradually during the discharge process. The increase is slow when the voltage is above 0.5 V (from 1.03 to 1.06), while it is fast when the voltage is below 0.5 V. Finally, the I_D/I_G value can reach 1.15 at 0.01 V. The increase in I_D/I_G is attributed to increased disordered structure produced by K⁺ insertion in the carbon layer [48, 49]. This result once again confirms that the potassium storage in the low-voltage

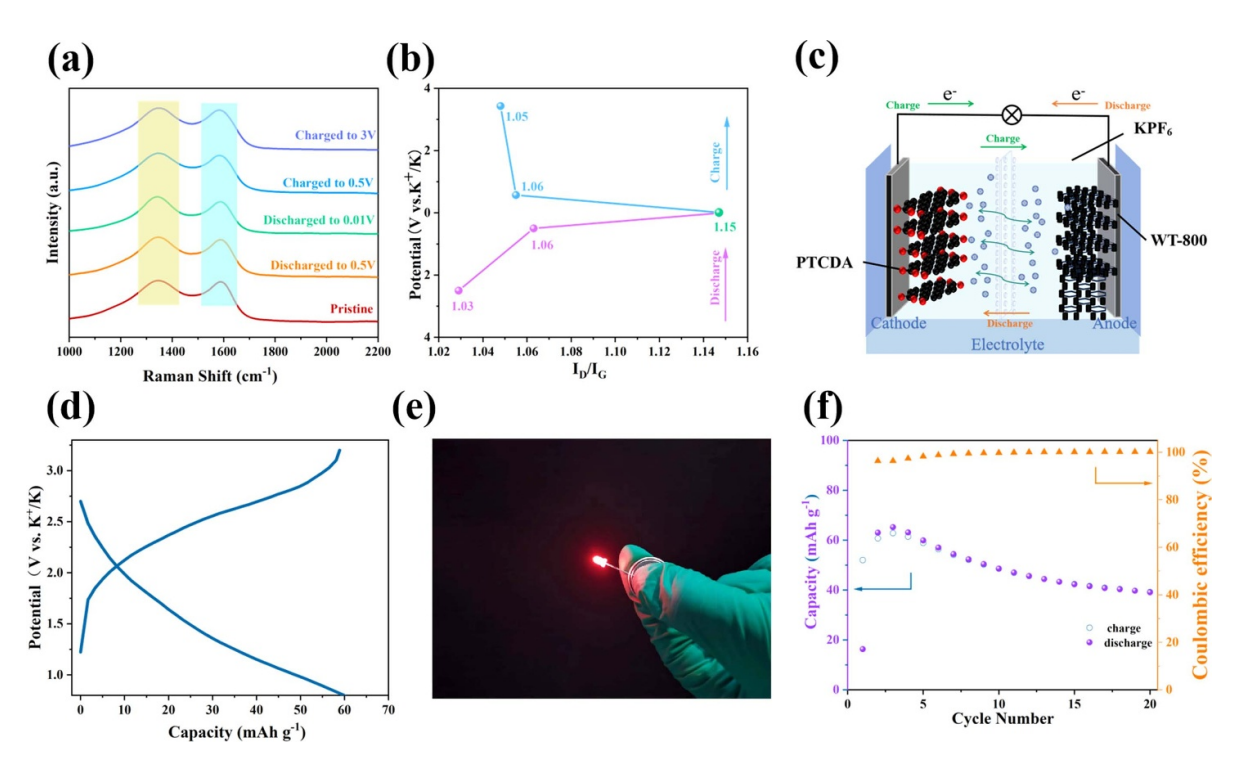


Figure 4. (a) Ex situ Raman spectra of WT-800 at different charge/discharge states and (b) the corresponding I_D/I_G values; (c) WT-800//PTCDA full cells (d) the charge/discharge profiles of WT-800//PTCDA full cells at 0.1 A g⁻¹, (e) optical photograph of a red LED lighted by the full cell, and (f) the cycling stability of the full cell at 0.1 A g⁻¹.

region is dominated by diffusion. Due to the extraction of K^+ between the carbon layers and the desorption of K^+ at defect sites, the I_D/I_G value gradually decreases during the charging process [50, 51]. At the end of the charge, the value recovers to 1.05, which is close to the initial value (1.04), indicating the structural reversibility of WT-800.

A full cell was assembled employing WT-800 as the anode and commercial PTCDA as the cathode (figure 4(c)). The morphological properties and electrochemical performance of PTCDA are presented in **figures** (**S11**) and (**S12**). Figure 4(d) shows the GCD profiles of the WT-800//PTCDA full cell. It can light up a red light-emitting diode (LED, 1.8–2.4 V) (figure 4(e)). After cycling 20 times at 0.1 A g $^{-1}$, the discharge capacity of the full cell keeps $\sim\!40$ mAh g $^{-1}$ (figure 4(f)), corresponding to an energy density of 60 Wh kg $^{-1}$ based on the total mass of the cathode and anode.

4. Conclusions

In this work, we utilized Platanus occidentalis L. fruit, a waste biomass material, as a precursor to synthesize an environmentally friendly biomass carbon anode for the first time and investigated its electrochemical performances in PIBs. As the carbonization temperature increases, the interlayer spacing gradually decreases while the degree of graphitization intensifies. When the temperature reached 800 °C, the material retained the porous structure inherent to the natural Platanus occidentalis L. fruit and exhibited a suitable interlayer spacing of 0.38 nm. This porous structure provides abundant

active sites, which facilitate the rapid insertion and extraction of potassium ions, thereby enhancing the charging and discharging efficiency. Furthermore, it mitigates volume changes, protects the structure, and prolongs the cycle life. Based on the above advantages, when the biomass carbon was used as a PIB anode, it delivered a discharge capacity of 193.3 mAh g^{-1} after 100 cycles at 0.1 A g^{-1} and 80.4 mAh g^{-1} after 300 cycles at 0.3 A g⁻¹. Our work not only opens up a new avenue for resource utilization of waste Platanus occidentalis L. fruit but also provides a promising low-cost PIB anode material that can be mass-produced, thus contributing to the development of green chemistry and sustainable energy storage technologies. In the future, we will improve the performance through various methods such as doping, heat treatment, and surface modification. We hope this work will bring discoveries and provide innovative ideas and strategies for developing biomass carbon anode materials.

Data availability statement

All data that support the findings of this study are included within the article (and any supplementary files).

Acknowledgments

This work was supported by the National Natural Science Foundation of China (51974188), the Education Department of Liaoning Province (JYTQN2023285), the Shenyang University of Technology (QNPY202209-4), the Key Laboratory of Functional Inorganic Material Chemistry

(Heilongjiang University, Ministry of Education), and the Science and Technology Department of Liaoning Province (2024-BSLH-172). Y X acknowledges the support of the Engineering and Physical Sciences Research Council (EP/V000152/1, EP/X000087/1), Leverhulme Trust (RPG-2021-138), and Royal Society (IEC\NSFC\223016). For the purpose of open access, the author has applied a Creative Commons Attribution (CC BY) license to any Author Accepted Manuscript version arising. The authors would like to thank Dr Fei Yuan (Hebei University of Science and Technology) for his helpful discussions.

Conflict of interest

There are no conflicts to declare.

ORCID iDs

Jiaxing Hao https://orcid.org/0009-0008-6814-9529
Yuhan Wu https://orcid.org/0000-0002-6288-2112
Yusheng Wu https://orcid.org/0000-0002-6424-0324
Yang Xu https://orcid.org/0000-0003-0177-6348

References

- [1] Ran Y, Xu C, Ji D, Zhao H, Li L and Lei Y 2024 Research progress of transition metal compounds as bifunctional catalysts for zinc-air batteries *Nano Res. Energy* 3 e9120092
- [2] Wu Y, Chen G, Wu X, Li L, Yue J, Guan Y, Hou J, Shi F and Liang J 2023 Research progress on vanadium oxides for potassium-ion batteries J. Semicond. 44 041701
- [3] Yuan F, Sun H, Zhang D, Li Z, Wang J, Wang H, Wang Q, Wu Y and Wang B 2022 Enhanced electron transfer and ion storage in phosphorus/nitrogen co-doped 3D interconnected carbon nanocage toward potassium-ion battery *J. Colloid Interface Sci.* 611 513–22
- [4] Zhu L, Wang Y, Wang M, Huang M, Huang Y, Zhang Z, Yu J, Qu Y, Li C and Yang Z 2022 High edge-nitrogen-doped porous carbon nanosheets with rapid pseudocapacitive mechanism for boosted potassium-ion storage *Carbon* 187 302–9
- [5] Xu F, Zhai Y, Zhang E, Liu Q, Jiang G, Xu X, Qiu Y, Liu X, Wang H and Kaskel S 2020 Ultrastable surface-dominated pseudocapacitive potassium storage enabled by edge-enriched N-doped porous carbon nanosheets *Angew*. *Chem.* 59 19628–35
- [6] Wu Y, Zhao Q and Wang Z 2024 Layered vanadium oxides: promising cathode materials for calcium-ion batteries *Chin. J. Struct. Chem.* 43 100271
- [7] Xia P, Li S, Yuan L, Jing S, Peng X, Lu S, Zhang Y and Fan H 2024 Encapsulating CoRu alloy nanocrystals into nitrogen-doped carbon nanotubes to synergistically modify lithium-sulfur batteries separator J. Membr. Sci 694 122395
- [8] Xia W, Ji F, Liu Y, Han Z, Li K, Lu J and Ci L 2024 Deciphering the potential of potassium-ion batteries beyond room temperature Sci. Bull. 69 3371–83
- [9] Huan W, Pingxian F, Fangbao F, Xuefeng Y, Dongjie Y, Wenli Z, Li N and Qiu X 2022 Lignin-derived carbon materials for catalysis and electrochemical energy storage Carbon Neutralization 1 277–97
- [10] Wang H, Peng H, Xiao Z, Yu R, Liu F, Zhu Z, Zhou L and Wu J 2023 Double-layer phosphates coated Mn-based oxide

- cathodes for highly stable potassium-ion batteries *Energy Storage Mater.* **58** 101–9
- [11] Anjan A, Bharti V K, Sharma C S and Khandelwal M 2023 Carbonized bacterial cellulose-derived binder-free, flexible, and free-standing cathode host for high-performance stable potassium-sulfur batteries ACS Appl. Energy Mater. 6 3042–51
- [12] Wu Y-H, Xia W-H, Liu Y-Z, Wang P-F, Zhang Y-H, Huang J-R, Xu Y, Li D-P and Ci L-J 2024 Tungsten chalcogenides as anodes for potassium-ion batteries *Tungsten* 6 278–92
- [13] Saroja A P V K, Wu Y and Xu Y 2024 Improving the electrocatalysts for conversion-type anodes of alkali-ion batteries Chin. J. Struct. Chem. 44 100408
- [14] Yang S, Zhang F, Ding H, He P and Zhou H 2018 Lithium metal extraction from seawater *Joule* 2 1648–51
- [15] Wu Y, Zhao Z, Hao X, Xu R, Li L, Lv D, Huang X, Zhao Q, Xu Y and Wu Y 2023 Cathode materials for calcium-ion batteries: current status and prospects *Carbon Neutralization* 2 551–73
- [16] Yang J, Zhai Y, Zhang X, Zhang E, Wang H, Liu X, Xu F and Kaskel S 2021 Perspective on carbon anode materials for K⁺ storage: balancing the intercalation-controlled and surface-driven behavior Adv. Energy Mater. 11 2100856
- [17] Ma L, Lv Y, Wu J, Xia C, Kang Q, Zhang Y, Liang H and Jin Z 2021 Recent advances in anode materials for potassium-ion batteries: a review *Nano Res.* 14 4442–70
- [18] Li D et al 2018 Facile fabrication of nitrogen-doped porous carbon as superior anode material for potassium-ion batteries Adv. Energy Mater. 8 1802386
- [19] Hosaka T, Kubota K, Hameed A S and Komaba S 2020 Research development on K-ion batteries *Chem. Rev.* 120 6358–466
- [20] Min X, Xiao J, Fang M, Wang W (Alex), Zhao Y, Liu Y, Abdelkader Amr M, Xi K, Kumar R V and Huang Z 2021 Potassium-ion batteries: outlook on present and future technologies *Energy Environ. Sci.* 14 2186–243
- [21] Huang S, Qiu X, Wang C, Zhong L, Zhang Z, Yang S, Sun S, Yang D and Zhang W 2023 Biomass-derived carbon anodes for sodium-ion batteries New Carbon Mater. 38 40–66
- [22] Yuan X, Zhu B, Feng J, Wang C, Cai X and Qin R 2021 Recent advance of biomass-derived carbon as anode for sustainable potassium ion battery *Chem. Eng. J.* 405 126897
- [23] Kaya A I 2024 Extraction of lightweight platanus orientalis L. fruit's stem fiber and determination of its mechanical and physico-chemical properties and potential of its use in composites *Polymers* 16 657
- [24] Yang Y, Zhou J, Rao A M and Lu B 2024 Bio-inspired carbon electrodes for metal-ion batteries *Nanoscale* **16** 5893–902
- [25] Chen N, Sabet M, Sapkota N, Parekh M, Chiluwal S, Koehler K, Clemons C M, Ding Y, Rao A M and Pilla S 2024 Bioderived silicon nano-quills: synthesis, structure and performance in lithium-ion battery anodes *Green Chem.* 26 4691–702
- [26] Antorán D, Alvira D, Peker M E, Malón H, Irusta S, Sebastián V and Manyà J J 2023 Waste hemp hurd as a sustainable precursor for affordable and high-rate hard carbon-based anodes in sodium-ion batteries *Energy Fuels* 37 9650–61
- [27] Zhang Y, Wang Z, Li D, Sun Q, Lai K, Li K, Yuan Q, Liu X and Ci L 2020 Ultrathin carbon nanosheets for highly efficient capacitive K-ion and Zn-ion storage *J. Mater.* Chem. A 8 22874–85
- [28] Wu Y, Wu X, Guan Y, Xu Y, Shi F and Liang J 2022 Carbon-based flexible electrodes for electrochemical potassium storage devices New Carbon Mater. 37 852–74
- [29] Li R, Huang J, Li J, Cao L, Zhong X, Yu A and Lu G 2020 Nitrogen-doped porous hard carbons derived from

- shaddock peel for high-capacity lithium-ion battery anodes *J. Electroanal. Chem.* **862** 114044
- [30] Wu S, Xu F, Li Y, Liu C, Zhang Y and Fan H 2023 Synergistically enhanced sodium ion storage from encapsulating highly dispersed cobalt nanodots into N, P, S tri-doped hexapod carbon framework *J. Colloid Interface* Sci. 649 741–9
- [31] Yang M, Dai J, He M, Duan T and Yao W 2020
 Biomass-derived carbon from ganoderma lucidum spore as a promising anode material for rapid potassium-ion storage *J. Colloid Interface Sci.* **567** 256–63
- [32] Wu F, Zhang M and Bai Y 2019 Lotus seedpod-derived hard carbon with hierarchical porous structure as stable anode for sodium-ion batteries ACS Appl. Mater. Interfaces 11 12554–61
- [33] Qiu C, Jiang L, Gao Y and Sheng L 2023 Effects of oxygen-containing functional groups on carbon materials in supercapacitors: a review *Mater. Des.* 230 111952
- [34] Zheng J, Yu K, Wang X, Liang J and Liang C 2023 Nitrogen self-doped porous carbon based on sunflower seed hulls as excellent double anodes for potassium/sodium ion batteries *Diam. Relat. Mater.* 131 109593
- [35] Huang H, Xu R, Feng Y Z, Zeng S F, Jiang Y, Wang H J, Luo W and Yu Y 2020 Sodium/potassium-ion batteries: boosting the rate capability and cycle life by combining morphology, defect and structure engineering Adv. Mater. 32 1904320
- [36] Xia G L, Wang C L, Jiang P, Lu J, Diao J F and Chen Q W 2019 Nitrogen/oxygen co-doped mesoporous carbon octahedrons for high-performance potassium-ion batteries J. Mater. Chem. A 7 12317–24
- [37] Li G, Chen S, Wang Y, Wang G, Wu Y and Xu Y 2023 N, S co-doped porous graphene-like carbon synthesized by a facile coal tar pitch-blowing strategy for high-performance supercapacitors *Chem. Phys. Lett.* 827 140712
- [38] Li D, Sun Q, Zhang Y, Dai X, Ji F, Li K, Yuan Q, Liu X and Ci L 2021 Fast and stable K-ion storage enabled by synergistic interlayer and pore-structure engineering *Nano Res.* 14 4502–11
- [39] Li X J, Yang C, Wang S Q, Mao X Y and Yu K F 2022 Comprehensive study on improving the sodium storage performance of low-defect biomass-derived carbon through S or N doping *Diam. Relat. Mater.* 129 109382
- [40] Xu Y, Zhang C, Zhou M, Fu Q, Zhao C, Wu M and Lei Y 2018 Highly nitrogen doped carbon nanofibers with superior rate

- capability and cyclability for potassium ion batteries *Nat. Commun.* **9** 1720
- [41] Wang C, Xue S, Lei X, Wen J, Pan X, Zhang F, Zou C and Tang Y 2023 Amidation structure design of carbon materials enables high energy and power density symmetric sodium-ion battery *Chem. Eng. J.* 470 144043
- [42] Wang D, Yang J, Li X, Geng D, Li R, Cai M, Sham T-K and Sun X 2013 Layer by layer assembly of sandwiched graphene/SnO₂ nanorod/carbon nanostructures with ultrahigh lithium ion storage properties *Energy Environ*. Sci. 6 2900–6
- [43] He H et al 2019 Anion vacancies regulating endows MoSSe with fast and dtable potassium ion storage ACS Nano 13 11843–52
- [44] Wang P, Gong Z, Ye K, Gao Y, Zhu K, Yan J, Wang G and Cao D 2021 Sulfur-doped biomass carbon as anode for high temperature potassium ion full cells *Electrochim. Acta* 374 137920
- [45] Wang P, Gong Z, Ye K, Gao Y, Zhu K, Yan J, Wang G and Cao D 2021 N-rich biomass carbon derived from hemp as a full carbon-based potassium ion hybrid capacitor anode *Appl. Surf. Sci.* 553 149569
- [46] Zhu T, Mai B, Hu P, Cai C, Xing B, Wei Z, Chen C, Fan H, Li M and Wang X 2023 Bagasse-derived hard carbon anode with an adsorption-intercalation mechanism for high-rate potassium storage ACS Appl. Energy Mater. 6 2370-7
- [47] Yan H, Huang X, Li H and Chen L 1998 Electrochemical study on LiCoO₂ synthesized by microwave energy Solid State Ion. 113 11–15
- [48] Bo Z et al 2024 Resolving the tradeoff between energy storage capacity and charge transfer kinetics of sulfur-doped carbon anodes for potassium ion batteries by pre-oxidation-anchored sulfurization Energy Storage Mater. 69 103393
- [49] Zhong G, Lei S, Hu X, Ji Y, Liu Y, Yuan J, Li J, Zhan H and Wen Z 2021 Facile synthesis of P-doped carbon nanosheets as Janus electrodes of advanced potassium-ion hybrid capacitor ACS Appl. Mater. Interfaces 13 29511–21
- [50] Guo R, Liu X, Wen B, Liu F, Meng J, Wu P, Wu J, Li Q and Mai L 2020 Engineering mesoporous structure in amorphous carbon boosts potassium storage with high initial coulombic efficiency *Nanomicro Lett.* 12 148
- [51] Ma X, Xiao N, Xiao J, Song X, Guo H, Wang Y, Zhao S, Zhong Y and Qiu J 2021 Nitrogen and phosphorus dual-doped porous carbons for high-rate potassium ion batteries Carbon 179 33–41